



Electrochemically roughened silver surface versus fractal leaf-shaped silver crystals for surface-enhanced Raman scattering investigation of polypyrrole

A. El Guerraf¹ · Z. Aouzal¹ · M. Bouabdallaoui¹ · S. Ben Jadi² · A. El Jaouhari² · R. Wang³ · M. Bazzaoui² · E.A. Bazzaoui¹

Received: 7 March 2019 / Revised: 31 March 2019 / Accepted: 26 April 2019 / Published online: 10 May 2019
© Springer-Verlag GmbH Germany, part of Springer Nature 2019

Abstract

In surface-enhanced Raman scattering (SERS) analyses, the surface condition of the metal substrate plays a decisive role in the quality of the recorded Raman spectra. In this contribution, we will examine the SERS spectra of polypyrrole (PPy) in contact with two types of silver substrates prepared according to two different protocols: (i) electrochemical, leading to Ag surface with coral-like structure, and (ii) photochemical, giving fractal leaf-shaped Ag clusters. On the one hand, PPy films were electrochemically synthesized on massive silver electrodes previously SERS-activated according to the well-known oxidation-reduction cycle (ORC) procedure. The Raman spectra of the obtained samples exhibit significant SERS effect with high signal-to-noise ratio in comparison with those recorded in the same conditions on platinum. This made it possible to perform an *ex situ* rovibrational characterization of PPy, to determine the orientation and anchoring mode of the polymer chains in the coating/electrode interfacial region, and to monitor, *in situ*, some structural changes during the electrochemical doping-undoping process. On the other hand, to further improve the SERS enhancement factor, a second photochemical approach has been developed to prepare PPy chains embedded in a fractal structure made of leaf-shaped silver crystals. Here, the size and growth mode of the silver clusters give rise to a larger number of “hot spots” that are responsible for the huge Raman intensity enhancement.

Keywords Polypyrrole · Surface-enhanced Raman scattering · Fractal silver crystals · Roughened silver electrodes

Highlights

- Analyses of PPy electrodeposited on roughened Ag electrode led to SERS spectra with 10^2 enhancement factor.
- SERS selection rules suggest that the inner PPy layers grow with the rings in “standing” position.
- Photochemical polymerization of pyrrole in AgNO_3 solution under UV irradiation led to SERS-active PPy-Ag composite.
- The fractal geometry of the silver crystals is responsible for the observation of a huge SERS effect.
- *In situ* SERS analysis of the $\nu_{\text{C}=\text{C}}$ mode revealed the contribution of two aromatic and quinoid components.

✉ E.A. Bazzaoui
bazzaoui@webmails.com

¹ Laboratoire de Chimie des Matériaux (LCM), Faculté des Sciences, Université Mohammed 1er, 60 000 Oujda, Morocco

² Laboratoire Matériaux et Environnement (LME), Faculté des Sciences, Université Ibn Zohr, 80 000 Agadir, Morocco

³ Department of Mechanical Systems Engineering, Faculty of Engineering, Hiroshima Institute of Technology, 2-1-1 Miyake, Saeki-ku, Hiroshima 731-5193, Japan

Introduction

Currently, nanotechnologies are increasingly interested in metallic nanoparticles, particularly silver ones because of their exceptional properties and the extent of their field of application. They are exploited in microbiology [1–4], catalysis [5–7], microelectronics [8–10], and, especially, in the analysis by surface-enhanced Raman scattering (SERS) [11–14].

SERS technique discovered in the mid-1970s [15] is based on the use of metals such as silver, gold, and less frequently copper, generally in the form of roughened massive substrates or particles in colloidal suspensions. Here, the size and shape of the asperities of the metal surface or colloidal aggregates play a key role in the emergence of the SERS effect and affect the value of the enhancement factor of the Raman intensity. In this context, it has been reported that the enhancement factor can reach values in the order of 10^{14} [16–20] which would make possible the detection of traces or even single molecule in complex environments such as biological media [21–26].

It has been shown in many studies that the amplification of the local electromagnetic field, due to surface plasmon resonance [27] and responsible for the enhancement effect, arises at intergranular sites, conventionally called “hot spots”, whose dimensions are smaller than the wavelength of the excitation line [28–34]. Hence, the current craze for controlled development of new metal nanomatrices including many “hot spots” with increasingly reduced dimensions [35, 36].

Drawing on this, one should expect to observe a huge intensification of the Raman signal for molecules adsorbed or electrodeposited on Ag or Au fractal clusters due to the presence of a large number of “hot spots” in this kind of structures with scale invariance symmetry [31–34]. This is the context in which our present paper fits.

Since several years, our research team is involved in the improvement and design of new systems origins of the SERS effect and their application to rovibrational investigations of electrosynthesized conducting polymers [37–43]. We have shown that this fine and powerful technique not only allows to provide precise information about the polymer structure and to follow the in situ changes occurring at the conjugated skeleton during the doping-undoping process, but also to access the spatial arrangement of the chains and their anchoring mode to the SERS-active surface. We have used (i) Ag, Au, and Cu electrodes previously activated by mechanical and electrochemical roughening procedures specific to each metal [37, 40–43]; (ii) partially aggregated Ag and Au colloids in the case of soluble conducting polymers [40, 42, 43]; (iii) multi-layer systems in which the polymer is either electrodeposited on a thin layer of a SERS-active metal coating a supporting metal plate or sandwiched between the thin SERS-active layer and the working electrode [41, 42]; and (iv) organized media based on micelles whose counterion is the Ag^+ cation [40, 42, 43]. Electropolymerization by cyclic scanning of potential in this electrolytic medium leads to the production of a composite polymer film containing entrapped Ag nanoparticles...

In the present work, and to focus on the influence of the fractal geometry of the SERS-active matrix on the Raman spectrum quality of a conducting polymer, we present a comparative SERS study between two polypyrrole films prepared according to two different protocols. The first protocol is electrochemical (ECP) and consists of electrodepositing a thin PPy film on an Ag electrode previously roughened by potentiodynamic oxidation-reduction cycles. In this case, to highlight the emergence of SERS effect and to evaluate the enhancement factor, a film electrodeposited under the same conditions on a Pt electrode is also analyzed. The second protocol is photochemical (PCP), in which the deposition of PPy is done by electron transfer between the pyrrole monomer and the Ag^+ cation present in the solution, which leads to a composite formed of polypyrrole with fractal Ag clusters. The reaction is photocatalyzed by UV light [44–46], and the formation of the silver fractal structure is accelerated by the

copper plate because of the large potential gap between the Cu^{2+}/Cu (ca. +0.34 V) and Ag^+/Ag (ca. +0.80 V) redox pairs. This last procedure gives rise to PPy SERS spectra of high quality and much more intense than those observed in the case of the electrochemical protocol.

Experimental

Chemicals

Pyrrole $\text{C}_4\text{H}_5\text{N}$ ($\geq 98\%$, Aldrich) was redistilled and stored in the dark under argon atmosphere prior to use. Anhydrous dichloromethane CH_2Cl_2 ($\geq 99.8\%$, Sigma-Aldrich) packaged under nitrogen in Sure/Seal™ bottle, silver nitrate AgNO_3 ($\geq 99.0\%$, Sigma-Aldrich), and potassium chloride KCl ($\geq 99.0\%$, Sigma-Aldrich) were used as received. Perchloric acid HClO_4 (11 M, Sigma-Aldrich) was diluted to 2 M with distilled water. Tetrabutylammonium hexafluorophosphate ($\geq 99.0\%$, Sigma-Aldrich) was dried under vacuum before each electrochemical experiment. Water was purified by passing distilled water through a Millipore purification system.

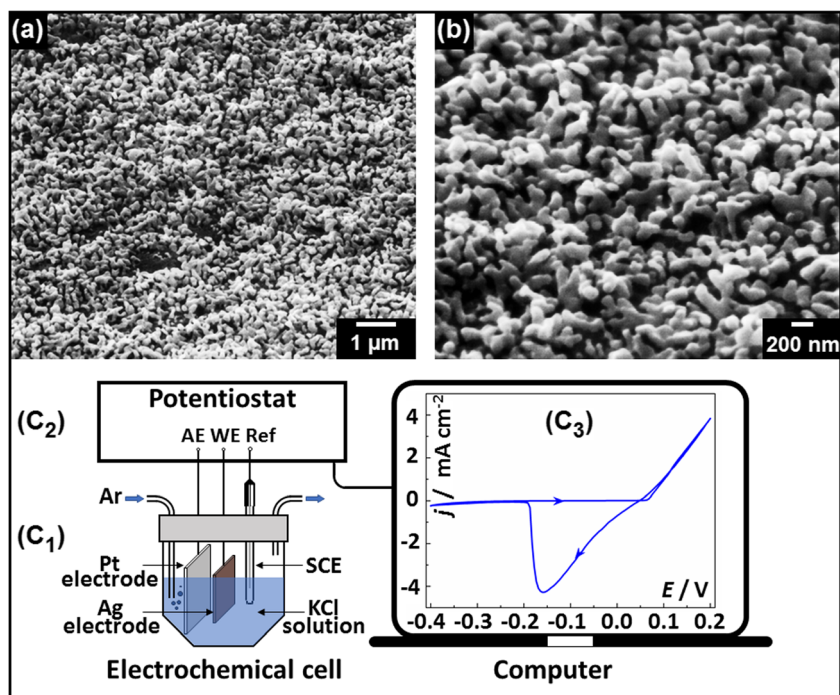
Preparation of the SERS-active samples

SERS effect only occurs if the underlying metal has undergone specific roughening mechanical, chemical, and/or electrochemical treatments. As in the case of metal colloids [47–54], SERS intensity is closely related to the shape and dimensions of the surface asperities. In what follows, we will describe two different protocols (ECP and PCP) for the preparation of SERS-active substrates. Then, to compare their enhancement factors, the two supports will be used for the investigation of polypyrrole.

In the ECP protocol, a preliminary roughening procedure is applied to an Ag electrode. Initially, a first rapid polishing is carried out using 1200 grit sandpaper, aiming to achieve the planeness of the metal surface, followed by a succession of three steps of fine polishing using 6, 3, and 1 μm diamond pastes, respectively. This mechanical pretreatment gives the Ag surface a shiny mirror-like finish.

The silver electrode is then introduced into an electrochemical cell containing 0.1 M KCl aqueous solution. Then, three potential sweeps between -0.4 and $+0.2$ V vs SCE are applied to the working electrode with 10 mV s^{-1} scan rate. The voltammogram corresponding to the oxidation-reduction cycle (Fig. 1) is characterized by an abrupt growth of the anodic current at $+0.1$ V which corresponds to the oxidation of the polished Ag surface and the formation of silver chloride. On the return, a cathodic peak appears at -0.15 V and corresponds to the reduction of the silver chloride deposited on the surface of the electrode.

Fig. 1 Electrochemical set-up used for roughening the silver electrode, comprising a single compartment electrochemical cell (**c₁**) equipped with a three-electrode system connected to a computer-controlled potentiostat (**c₂**). The potentiodynamic curve (**c₃**) and SEM micrographs of the electrode surface (**a**, **b**) obtained after the SERS-activation procedure are also shown



Thus, the consecutive and repetitive dissolution-redeposition of silver creates topographic defects on the electrode surface which are responsible for the SERS effect produced by excitation of the surface plasmons. The micrograph obtained by scanning electron microscopy (SEM) shown in Fig. 1 is that of the Ag electrode after the electrochemical activation treatment. The surface asperities are in the form of spheroids bonded to each other to form rods that themselves form connections in a “coral-like” structure whose distribution is uniform over the entire surface of the electrode.

The PCP protocol is based on an in situ oxidation of pyrrole by Ag^+ cations on a copper plate in aqueous solution of silver nitrate and under UV irradiation: A carefully polished copper plate is introduced into 0.5 M aqueous pyrrole solution. Then, under constant stirring and UV exposure (365 nm), a silver nitrate solution AgNO_3 0.2 M is slowly added dropwise. The procedure takes about an hour and can also be performed under daylight without UV lamp; in this case, a longer time is required for polymerization (more than 24 h). The used concentrations and operating conditions were retained after several optimization tests. An electronic transfer occurs between the monomer and the Ag^+ cations and leads to a photo-assisted chemical polymerization of pyrrole and at the same time to a deposit of Ag^0 particles on the electrode surface.

Topographic analysis of the electrode surface reveals a particular structure of the silver deposit. On the micrograph of Fig. 2, the growth of the Ag clusters is done by repetition of the same “pine leaves” forms at increasingly smaller scales, giving a fractal geometry on the surface of the Cu plate. The

importance of the fractal behavior in the observation of SERS effect has been shown by several authors [47, 48, 55–60].

During the formation of a PPy chain of length $n (=l \times k)$, the photochemical polymerization follows the Scheme 1 below: where j, k, l, m , and n are the non-zero positive integers: $n = l \times k$ is the average chain length, $1/l$ represents the doping rate ($\approx 33\%$ for fully doped PPy), and $j = m \cdot k$.

Generally, the obtaining of a fully doped polymer involves about 2.33 electrons for each monomer unit: $2 e^-$ removed to allow coupling in the two α and α' positions and $0.33 e^-$ corresponding to the fraction of the positive charge carried by the ring and compensated by one doping anion for each three monomer units. The reaction leads to the formation of a PPy-Ag composite doped with nitrate anions NO_3^- . Nitric acid is also obtained as bypass product.

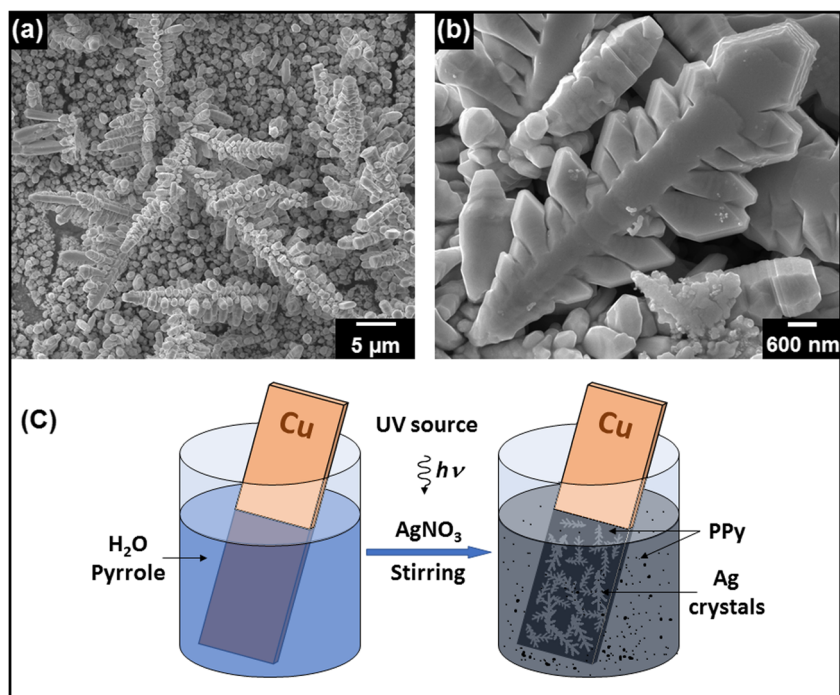
Electrochemical apparatus and characterization techniques

Electrochemical apparatus

The potentiodynamic and galvanostatic electrochemical experiments were carried out in a one-compartment cell using a Voltalab potentiostat/galvanostat model PGZ-301. The working electrode (WE) was either platinum or roughened silver plates (40 mm \times 8 mm). The auxiliary electrode (AE) was a stainless-steel grid and potentials were measured vs. SCE reference electrode (Ref).

The in situ SERS experiments were performed using a homemade Teflon micro cell equipped with three miniaturized

Fig. 2 Schematic representation of the photochemical procedure (c) used for the preparation of polypyrrole with embedded fractal leaf-shaped silver crystals on a copper plate. The SEM micrographs (a, b) obtained at the end of the experiment show the growth geometry of the silver matrices responsible for the huge SERS effect



electrodes: WE was a SERS-activated silver disk ($\varnothing = 4$ mm) coated with a thin PPy layer. A stainless-steel cap-shaped grid with a small circular aperture at its center to allow the passage of the excitation laser beam served as AE. A thin silver wire ($\varnothing = 0.25$ mm) covered with silver chloride (Ag/AgCl) was used as reference electrode.

Raman spectroscopy

Raman spectra were recorded using $\lambda_e = 514.5$ nm excitation green line from of a Spectra-Physics model 165 argon ion laser. The scattered light, collected at 180° from the incident beam (retro-Raman), was focused onto the entrance slit of a Dilor XY spectrometer. This apparatus consists of a double monochromator used in subtractive mode (i.e., with no dispersion) to select a given spectral range, followed by a spectrograph to complete the dispersion and by a 1024×256 Jobin-Yvon CCD matrix multichannel detector, cooled by the thermoelectric effect.

X-ray photoelectron spectroscopy

XPS analyses were performed with a Vacuum Generators Escalab MKI spectrometer equipped with Mg $K\alpha$ (1256.6 eV) and Al $K\alpha$ (1486.6 eV) sources operating at

200 mW. X-rays, focused onto an area of $4 \text{ mm} \times 10 \text{ mm}$, are weak enough not to damage the sample. Spectra were calibrated against the 1 s carbon electron peak (285 eV binding energy) of the polythiophene ring carbon atoms as internal reference.

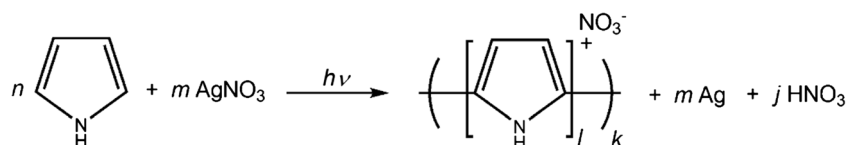
Results and discussion

SERS analysis of PPy electrodeposited on roughened silver electrode

The electropolymerization of pyrrole was carried out on Pt and Ag electrodes by the galvanostatic method at 0.5 mA cm^{-2} current density, in $\text{CH}_2\text{Cl}_2 + 0.1 \text{ M N}(\text{Bu})_4\text{PF}_6 + 0.1 \text{ M pyrrole}$ electrolytic medium. Beforehand, the silver electrodes were subjected to mechanical polishing and electrochemical activation treatments according to the aforementioned ECP protocol.

In order to prevent the oxidation of the silver electrode which would hinder the pyrrole polymerization reaction, the constituents of the electrolytic medium have been carefully selected after tests carried out on several solvents and supporting electrolytes. A total of 0.5 mA cm^{-2} is the threshold value that leads to the formation of a PPy without

Scheme 1 Photochemical polymerization of pyrrole by AgNO_3



exceeding the oxidation potential of the monomer (0.8 V) (Fig. 3b, c). The obtained film is electroactive and its electroactivity voltammogram is characterized by a couple of well-defined oxidation and reduction peaks at -0.05 and -0.40 V, respectively (Fig. 4). Values below 0.5 mA cm^{-2} do not allow electropolymerization (Fig. 3a), while high values ($> 1 \text{ mA cm}^{-2}$) give poor quality films since the electropolymerization plateaus occur at high potentials (Fig. 3d, e) for which the polymer is overoxidized and undergoes partial degradation [61–64].

Ex situ SERS experiments

Ex situ Raman analysis of the PPy films covering the two metal substrates with $\lambda_e = 514.5 \text{ nm}$ excitation wavelength reveals great differences. Since platinum is not a SERS-active material, the Raman spectrum obtained on this metal with 10 mW laser power is of weak intensity (Fig. 5). On the other hand, the film deposited on roughened Ag shows a very important SERS effect; the spectrum recorded in this case with reduced laser power (1 mW) is more intense with better resolved peaks (Fig. 5). By comparing the intensities of the most intense band in the two spectra, considering the laser powers used in each case, the SERS enhancement factor was evaluated at ca. 100.

Moreover, all bands observed on Pt electrode are present when the Ag electrode is used. In addition, thanks to the SERS effect, other vibrational modes, inactive on Pt, are visible on the spectrum obtained on Ag.

As can be seen from Fig. 5, the Raman spectra of PPy, recorded on Pt and activated Ag electrodes, respectively, have overall same behaviors. The SERS spectrum is dominated by intense and broad signals in the $1200\text{--}1600 \text{ cm}^{-1}$ domain. The

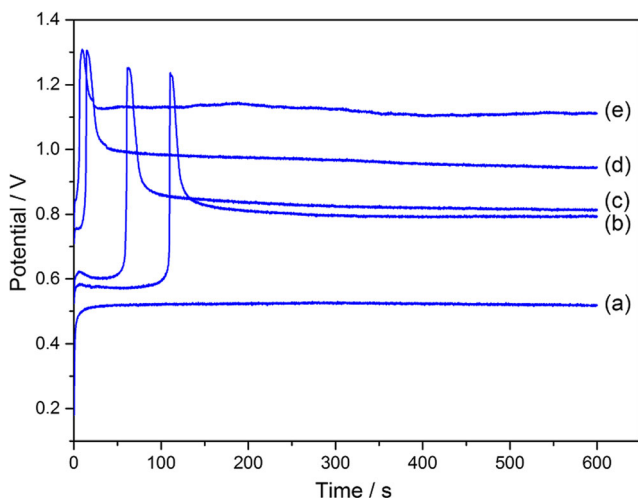


Fig. 3 Chronopotentiometric curves recorded during pyrrole electropolymerization in $\text{CH}_2\text{Cl}_2 + 0.1 \text{ M N}(\text{Bu})_4\text{PF}_6 + 0.1 \text{ M}$ pyrrole electrolytic medium on SERS-activated Ag electrode. Applied current densities: **a** 0.1 mA cm^{-2} , **b** 0.5 mA cm^{-2} , **c** 1 mA cm^{-2} , **d** 2 mA cm^{-2} , and **e** 5 mA cm^{-2}

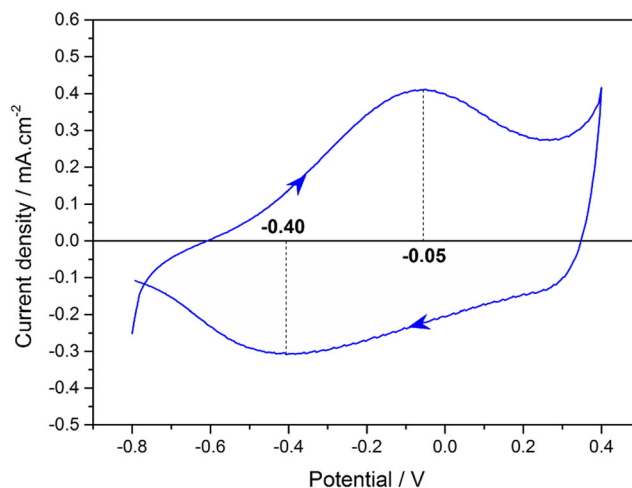


Fig. 4 Electrochemical behavior of polypyrrole film recorded in $\text{CH}_2\text{Cl}_2 + 0.1 \text{ M N}(\text{Bu})_4\text{PF}_6$ electrolytic medium with 20 mV s^{-1} scan rate. PPy was obtained galvanostatically on SERS-activated Ag electrode with 0.5 mA cm^{-2} current density

asymmetrical shapes of their envelopes suggest that they result from the overlapping of several vibrational modes. Table 1 gathers the wavenumbers of the various vibrational modes pointed on the spectra of PPy/Pt and PPy/Ag with those calculated by Faulques et al. [65] using valence force field. The bands observed in the spectra were assigned according to literature.

The main band at ca. 1610 cm^{-1} is assigned to C=C ring stretching [65]. It is well known that the transition between the reduced and oxidized states of polypyrrole during the doping process is accompanied by the transformation of some rings from the aromatic to the quinoid structures. According to theoretical values reported by Faulques et al. [65], the frequency of the C=C stretching vibration in the quinoid nuclei is higher than that of the same vibrational mode belonging to the

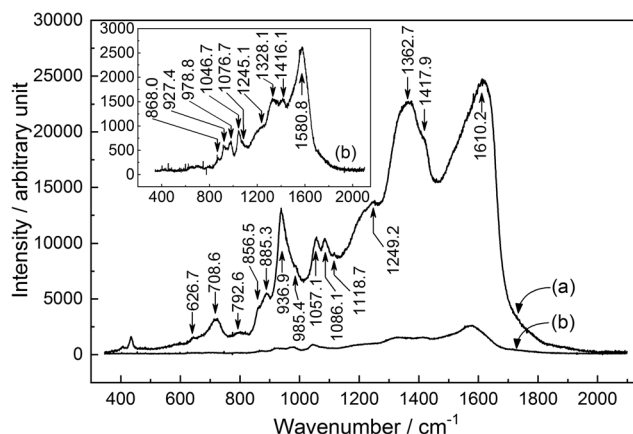


Fig. 5 SERS spectrum of polypyrrole film electrodeposited on roughened silver electrode **(a)** as compared to Raman spectrum of polypyrrole film electrosynthesized in the same conditions on platinum electrode **(b)**. The inset is the same as **b**. Excitation wavelength: $\lambda_e = 514.5 \text{ nm}$. Laser power: 10 mW in the case of Pt and 1 mW for roughened Ag

Table 1 Wavenumbers and assignments of the Raman bands of PPy films electrodeposited on Pt and roughened Ag electrodes, as compared to the calculated ones [65]

Experimental wavenumbers/cm ⁻¹		Calculated wavenumbers/cm ⁻¹ [65]		Assignments
PPy/Pt	PPy/Ag	Aromatic	Quinoid	
1580.8	1610.2	1563.2	1676.6	C=C ring stretching
1416.1	1417.9	1527.4	1524.4	C–N stretching
1328.1	1362.7	1316.5	1307.2	C–N antisym. Stretching
1245.5	1249.2			C–H antisym. in plane bending
	1118.7			
1076.7	1086.1			C–H in plane deformation
1046.7	1057.1	1043.4	1049.4	C–H in plane deformation
978.8	985.4	993.7	955.8	Ring in plane deformation
927.4	936.9			C–H stretching
	885.3			
868.0	856.5			C–H out of plane deformation
	792.6			
	708.6			
	626.7			Ring out of plane deformation

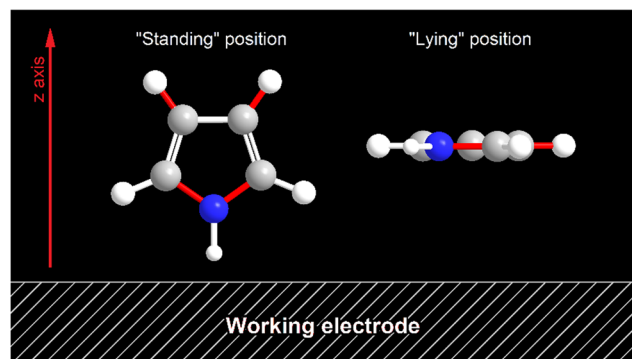
aromatic rings (Table 1). Therefore, by comparing the positions of the Raman bands of PPy/Pt and PPy/Ag spectra and particularly the $\nu_{C=C}$ main band, which is more shifted towards high frequencies in the case of PPy/Ag, it appears that the polymer deposited on Ag contains more quinoid nuclei than that elaborated on Pt. Therefore, because the number of quinoid units increases at the expense of aromatic ones when the oxidation degree of the polymer increases, PPy on Ag would be more oxidized than on Pt.

The bands observed around 1362, 1249, and 985 cm⁻¹ are assigned to the ring deformation, antisymmetric C–N stretching, antisymmetric C–H in plane bending, and ring in plane deformation. These bands have been reported to be due to bipolarons which are dications extended over three or four pyrrole nuclei of quinoid structure [66].

The double peaks of C–H in plane deformation at 1086 and 1057 cm⁻¹ were investigated by Liu and Hwang [67]. The authors stated that the intensity ratio of the two bands that form the doublet reflects the oxidation state of the polymer. When the oxidation degree is decreased, the intensity of the peak located at the higher wavenumber side of the doublet decreases and almost disappears for fully reduced PPy [67]. In our case, by qualitatively comparing the relative intensities of these two bands in the spectra of PPy/Ag and PPy/Pt (Fig. 5), it appears that the film on roughened silver is more oxidized than that on platinum, in agreement with the behavior of the $\nu_{C=C}$ main band explained above. This very important observation will be verified in the in situ SERS section.

In addition, two bands are particularly affected by the effect of intensity enhancement, the 937 and 1418 cm⁻¹ bands attributed to the C_β–H and C_α–N stretching modes, respectively. Taking the SERS selection rules into account, an approach to the spatial orientation of the pyrrole cycles with respect to

the metal surface can be made. Indeed, these rules predict that the most enhanced modes are those involving a significant variation of the α_{zz} component (along the oz axis normal to the surface of the SERS-active substrate) of the polarizability tensor during their vibration. This implies that the polypyrrole chains are oriented so that the C_β–H and C_α–N bonds form almost a right angle with the metal surface. Therefore, the pyrrole rings would be nearly in “standing” position, since they belong to the same plane as these bonds (Scheme 2). In previous works devoted to the investigation of polythiophene and its derivatives using activated Ag or Au electrodes or metal colloids, we have observed the same orientation of thiophene cycles with respect to the metal surface [37, 41, 42]. It should be noted that the same “standing” orientation was reported by Ye et al. [68] in a paper dedicated to surface-enhanced infrared absorption (SEIRA) investigation of polypyrrole-coated silver nanoparticles, albeit with the nitrogen atoms of the pyrrole rings pointing towards the outside of the PPy shell. However, the strong affinity of metals (Ag, Au,

**Scheme 2** Spatial representation of pyrrole units in “standing” and “lying” positions with respect to the SERS-active surface

...) for heteroatoms such as nitrogen and sulfur [69–77] corroborates with our observation.

The marked improvement of the Raman signal obtained using a roughened silver plate as working electrode for the electrosynthesis of PPy allowed the observation of high-quality SERS spectra and facilitated the identification of various vibrational modes of the polymer. Consequently, these operating conditions seem favorable for performing in situ SERS experiments coupling Raman spectroscopy to electrochemical techniques. Since the SERS effect only affects the inner layers of the polymer in direct contact with the metal substrate, the contribution of the vibrational modes of the electrolytic medium (solvent + supporting electrolyte) crossed by the laser beam will be negligible.

In situ SERS experiments

PPy film electrodeposited on roughened Ag electrode was polarized at various potentials in HClO_4 2 M aqueous medium and excited with green excitation line, $\lambda_c = 514.5$ nm, with only 1 mW laser power. Figure 6 illustrates the applied potential-time function ($E = f(t)$) and the resulting chronoamperometric response ($j = f(t)$). Despite a drop in intensity related to the in situ conditions, the overall aspect of the obtained spectra at different oxidation degrees (Fig. 7) is similar to that of the open-circuit ex situ spectrum.

All the bands described in the ex situ SERS analysis are also observed in the spectra recorded during the in situ procedure. A first comparative analysis of the SERS spectra overlaid on Fig. 7 reveals several modifications in the shapes, the positions, and the relative intensities of the bands.

When the potential of the working electrode is increased, the oxidation degree of the PPy film increases and leads to the creation of polarons (cation radicals) and bipolarons (dications) along the polymer chains. These charged entities, responsible for the conduction in the polymer, each consist of

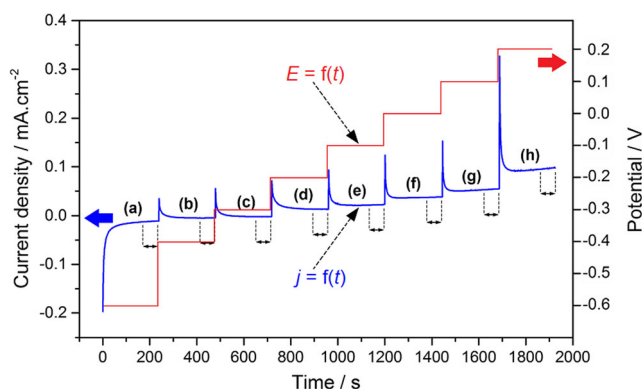


Fig. 6 Chronoamperometric response $j = f(t)$ obtained during the in situ SERS experiment. The double-arrows delimit the recording duration of each SERS spectrum. The applied potential-time function $E = f(t)$ is also shown. **a** – 0.6 V, **b** – 0.4 V, **c** – 0.3 V, **d** – 0.2 V, **e** – 0.1 V, **f** 0.0 V, **g** 0.1 V, and **h** 0.2 V vs Ag/AgCl

three to four quinoid-structured pyrrole units, resulting from transformation of an increasing number of aromatic-like pyrrole nuclei. This process is accompanied by the insertion of counter-ions from the electrolytic medium to ensure electro-neutrality. This results in distortions and conjugation ruptures in the chains and increases the disorder in the polymer.

To highlight these structural transformations, it is necessary to perform a detailed analysis of some PPy key bands, to identify those most affected by the SERS enhancement effect, and to follow their evolution depending on the oxidation degree.

Nevertheless, the overall raw spectra in Fig. 7 are difficult to interpret because they consist of bands, most of which are asymmetric or include shoulders, which implies that they consist of several overlapping lines. It is therefore useful to proceed with the deconvolution of these spectra in order to access information relating to the structural changes, the geometry, and the anchoring mode of the polymer to the metal surface. For reasons of simplification, the spectral range is divided into three zones denoted H, M, and L corresponding to high, medium, and low wavenumber domains, respectively (Fig. 7).

In zone H, the first observation concerns the most intense band $\nu_{C=C}$. When the PPy film is progressively doped, this band shifts towards high frequencies while widening. The plot representing the evolution of the $\nu_{C=C}$ wavenumber as a function of the polarization potential (Fig. 8) shows two characteristic regions. The first potential zone, between –0.4 and –0.25 V vs Ag/AgCl, takes the form of a plateau in which the $\nu_{C=C}$ band keeps a relatively fixed position. The second domain starts at ca. –0.25 V and is characterized by a linear variation of $\tilde{\nu}$ versus E with a positive slope of about $17.5 \text{ cm}^{-1} \text{ V}^{-1}$. Here, it should be noted that this behavior is not limited to 0.2 V as the upper limit imposed by the low oxidation potential of the Ag electrode, but continues beyond this value; suffice it to note the position of this band for the oxidized sample analyzed ex situ (Fig. 5).

Bukowska and Jackowska [78] have assigned the frequency shift of this band to the charge quantity introduced by doping into the polymer chains. These authors have assumed that the force constants of the pyrrole units forming the polymer could be sensitive to the electron density on the rings, which depends on the oxidation state of the polymer.

The second interesting feature of this band is its widening when the potential imposed to the working electrode increases. At first sight, this enlargement could be associated with changes in the distribution of the conjugation length in agreement with the work of Kuzmany et al. on polyacetylene [79, 80]. Indeed, the higher the doping rate of the polymer increases, the larger the number of structural defects on its chains becomes, thus causing a non-uniform distribution of the conjugated segments and leading to wider Raman bands. However, a second hypothesis seems more appropriate to explain both the shift and widening of this band: further analysis

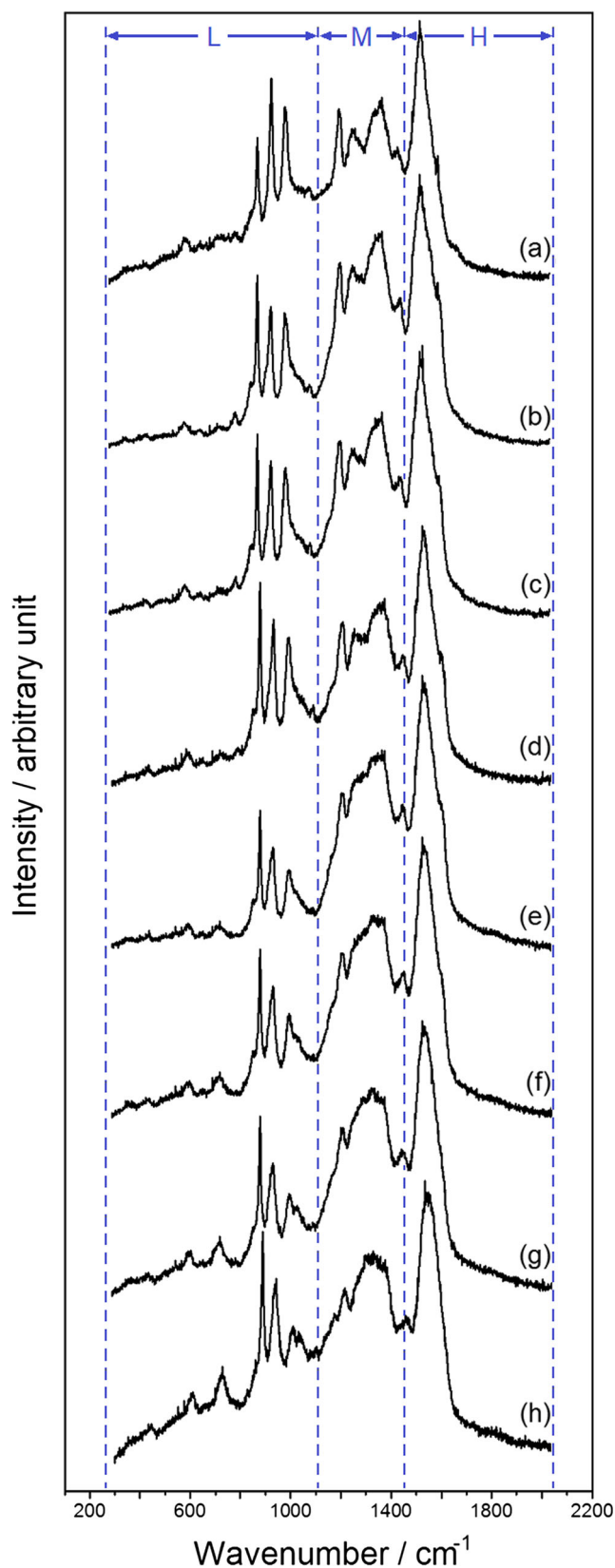


Fig. 7 Evolution of the in situ SERS spectrum of polypyrrole electrodeposited on roughened silver electrode as a function of the applied potential: **a** – 0.6 V, **b** – 0.4 V, **c** – 0.3 V, **d** – 0.2 V, **e** – 0.1 V, **f** 0.0 V, **g** 0.1 V, and **h** 0.2 V vs Ag/AgCl. Electrolytic medium: H₂O + 2 M HClO₄. Excitation wavelength: 514.5 nm. Laser power: 1 mW

changes with the applied potential (Fig. 9). This massif is, in fact, made up of the overlapping of at least two lines that we have attributed to the same stretching mode of C=C double bonds belonging to the nuclei of aromatic and quinoid structures.

When the Ag electrode is brought to increasing potentials, the oxidation degree of PPy increases and the number of nuclei which pass from the aromatic to the quinoid form becomes larger. This change in nuclei structure is reflected in the SERS spectrum by a growth of the high-frequency shoulder at the expense of the low-frequency component (Fig. 9).

It is well known that PPy spontaneously oxidizes in air, which implies that all spectra recorded ex situ are those of the oxidized form of PPy. This is verified by a simple observation of the $\nu_{C=C}$ band in the ex situ SERS spectrum (Fig. 5); on the one hand, it is very displaced towards the high frequencies and on the other hand its low-frequency side is characterized by a less steep slope than its high-frequency side, which means that in this case, the component $\nu_{C=C}^{quin.}$ is more intense than the component $\nu_{C=C}^{arom.}$.

The combination of these data concerning the position of $\nu_{C=C}$ signal and the intensity ratio of its two aromatic and quinoid components could be used as a criterion for evaluating the oxidation state of the polymer. However, it is necessary to take into consideration other parameters such as the electroynthesis conditions including the electrochemical method and the various constituents of the electrolytic medium, especially the nature of the doping anion which has been shown to strongly influence the behavior of the Raman spectrum [81, 82].

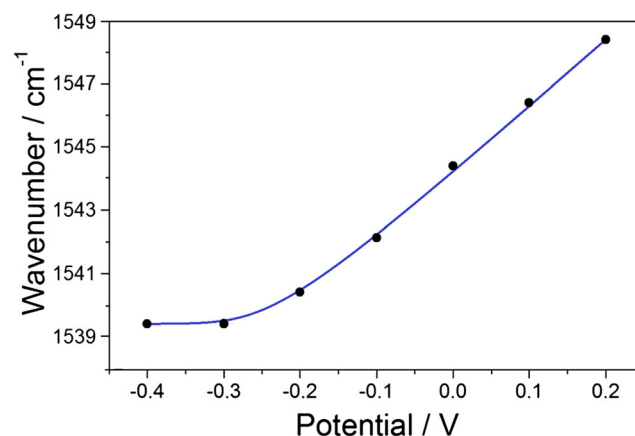
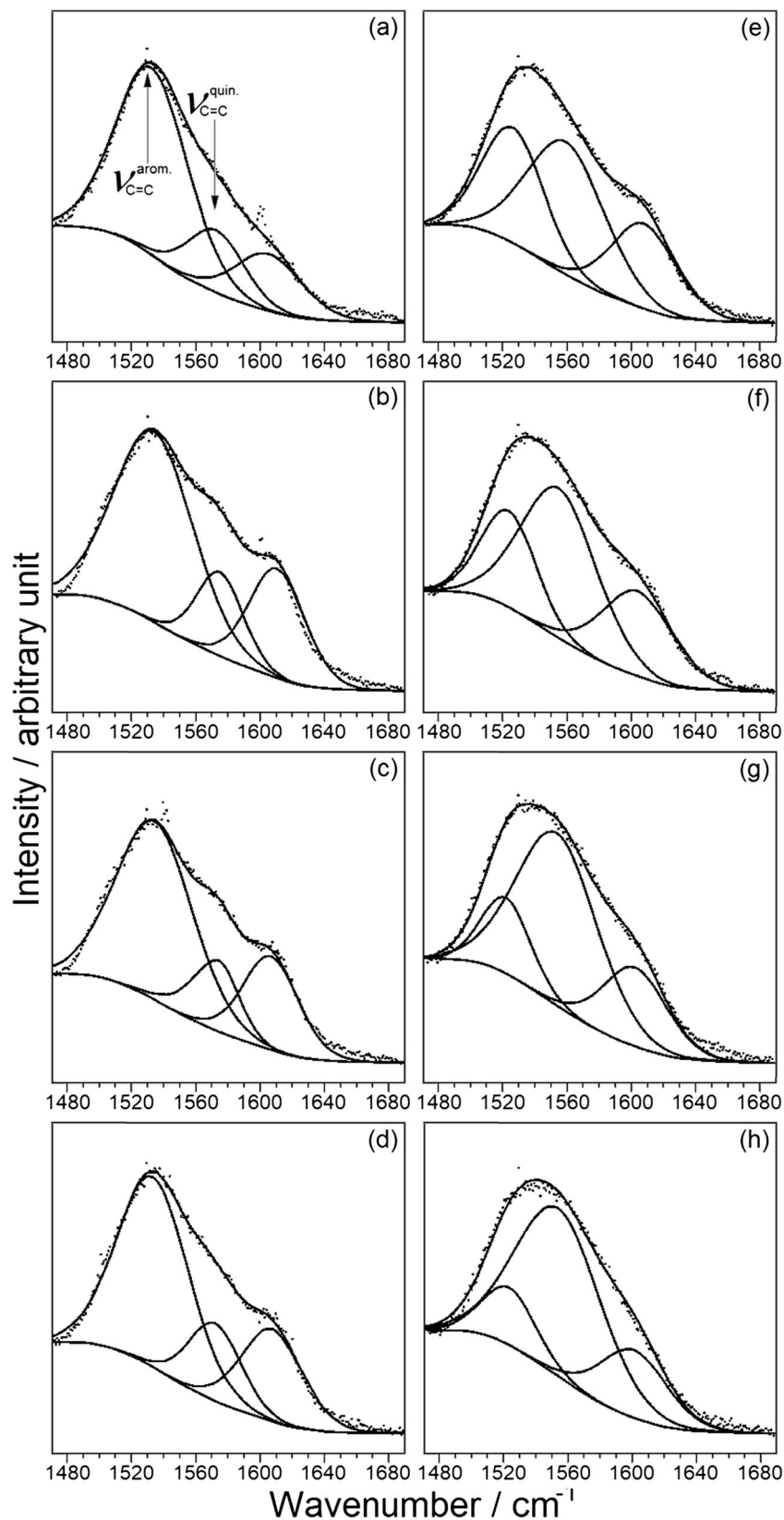


Fig. 8 Plot of $\nu_{C=C}$ wavenumber as a function of the polarization potential during the in situ SERS experiment. $\nu_{C=C}$ is assigned to stretching vibration of the C=C double-bonds of pyrrole rings

of the $\nu_{C=C}$ band reveals the existence of a shoulder on the high-frequency side of the main band and whose profile

Fig. 9 In situ evolution of the Gaussian components of the 1480–1680 cm^{-1} spectral region with the applied potential. The in situ experiment is performed in $\text{H}_2\text{O} + 2 \text{ M HClO}_4$ with 514.5 nm excitation wavelength and 1 mW laser power. Applied potentials: **a** -0.6 V , **b** -0.4 V , **c** -0.3 V , **d** -0.2 V , **e** -0.1 V , **f** 0.0 V , **g** 0.1 V , and **h** 0.2 V vs Ag/AgCl



In zone M, deconvolution and interpretation of the SERS signal are not straightforward since several bands, most often

broad, falls within this narrow wavenumber range. The poorly resolved M massif, with multiple overlapping components,

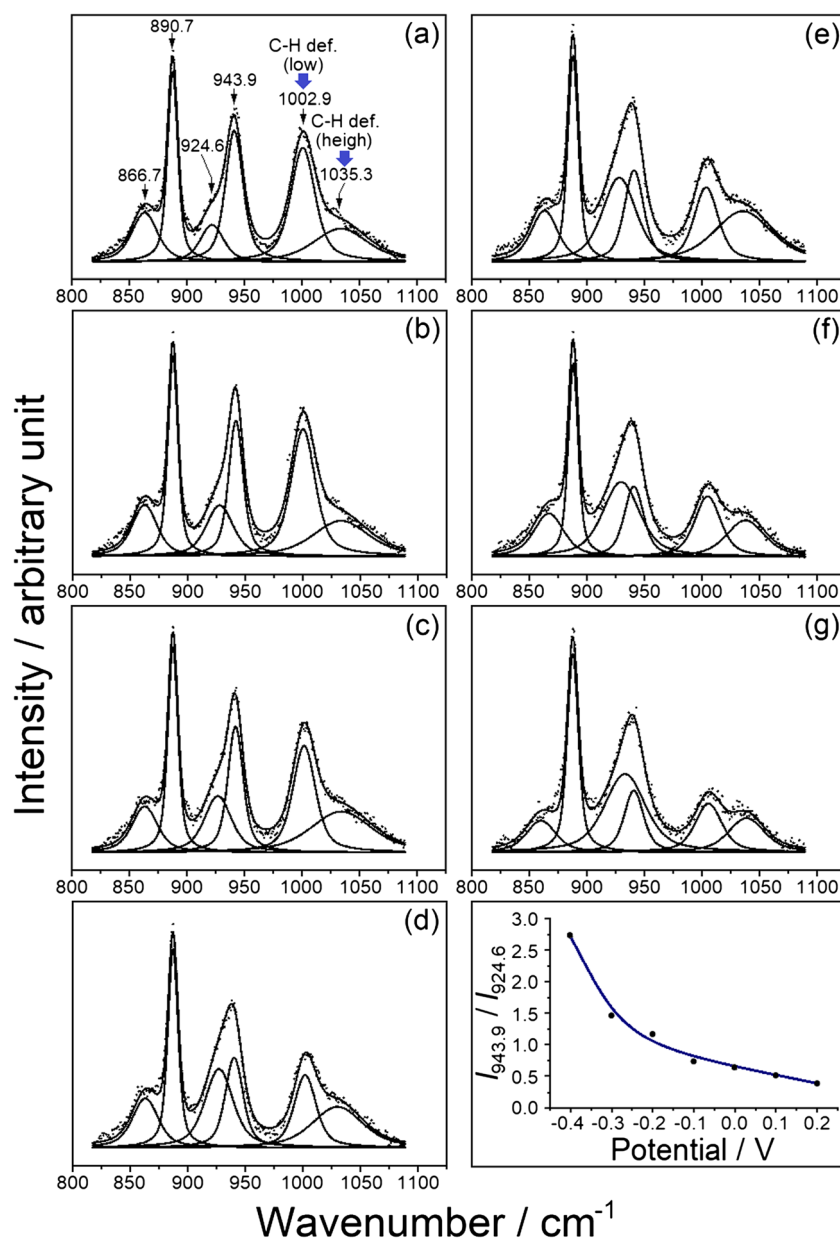
includes in addition to the normal modes indicated in Table 1, other modes probably due to vibrations of structural defects. The presence of the defect bands is supported by the evolution of the spectrum behavior in this domain (Fig. 7). In the reduced state (spectrum (a)), the bands are relatively sharp and less overlapped. But as soon as the oxidation degree is increased, the bands tend to widen and overlap in a broad and noisy envelope (spectrum (h)). This is the signature of the growth of disorder in the polymer chains.

Zone L mainly consists of three sharp and intense peaks in addition to three other low intensity bands revealed by a spectral decomposition procedure (Fig. 10). Modifications depending on the applied potential are observed essentially at the relative intensities of the different peaks. We must

especially notice the behavior of the double peaks of C–H in plane deformation (Fig. 10). As stated above, when the oxidation degree is decreased, the intensity of the peak located at the higher wavenumber side of the doublet decreases and almost disappears for fully reduced PPy [67]. This is exactly what we observe on Figs. 7 and 10: the intensity ratio of the two high- and low-frequency components $I_{\text{C-H}}^{\text{high}}/I_{\text{C-H}}^{\text{low}}$ increases when the applied potential is changed to more positive values.

In this spectral zone, besides the C–H in plane deformation doublet, other bands show changes. By way of indication, we have illustrated on the same Fig. 10 the variation of the intensity ratio $I_{943.9}/I_{924.6}$ of the 943.9 cm^{-1} (ring in plane deformation) and 924.6 cm^{-1} (C–H stretching) cm^{-1} lines as a

Fig. 10 In situ evolution of the Gaussian components of the 800–1100 cm^{-1} spectral region with the applied potential. The in situ experiment is performed in $\text{H}_2\text{O} + 2 \text{ M HClO}_4$ with 514.5 nm excitation wavelength and 1 mW laser power. Applied potentials: **a** –0.4 V, **b** –0.3 V, **c** –0.2 V, **d** –0.1 V, **e** 0.0 V, **f** 0.1 V, and **g** 0.2 V vs Ag/AgCl. The lower-right curve illustrates the evolution of the intensity ratio $I_{943.9}/I_{924.6}$ of the 943.9 and 924.6 cm^{-1} lines with the electrode potential



function of the electrode potential. The resulting curve can be divided into two domains, the first extending from -0.4 to about -0.25 V is characterized by a rapid decrease of the intensity ratio, and the second starting from -0.25 V has a softer slope.

The bands whose intensity increases during the doping process could be related either to a splitting due to the growth of the quinoid component at the expense of the aromatic one, or to the emergence of bands related to structural defects (*kinks*) and which have identified and investigated in in situ SERS experiments on polythiophene and its derivatives [37–42].

Moreover, it should be noted that the middle signal centered at about 930 cm^{-1} has been attributed by some authors to the symmetric stretching of the ClO_4^- doping anion [83, 84]. Therefore, its intensity should increase with the increase of the oxidation degree associated with the insertion of a growing number of counter-ions. However, on the in situ SERS spectra (Figs. 7 and 10), an inverse behavior occurs: on the one hand, the signal is present even in the fully reduced state, and on the other hand, its relative intensity decreases slightly when the potential of the working electrode is increased. These observations call into question the assignment of this band to the perchlorate doping anion.

SERS analyses of photochemically prepared PPy with leaf-shaped Ag crystals

Elemental composition of PPy containing Ag particles with leaf-like structure

X-ray photoelectron spectroscopy (XPS) is used for the characterization of PPy-Ag composite. Through this technique, which has proved to be a powerful tool in the analysis of conducting polymers, we will attempt to answer some issues about the chemical composition of the polymer, its doping level, the nature of the doping anion, and the oxidation state of the silver particles. This will be done by deconvoluting the XPS signals of carbon C1s, nitrogen N1s, and silver Ag3d. The first two elements will allow, by comparison of relative intensities, to access the PPy structure, to prove the involvement of the NO_3^- oxidizing species in the doping process, and to evaluate the doping degree. The third element will allow to verify that the silver particles responsible for the SERS effect are in the metallic state Ag^0 .

Elemental analysis by XPS of Ag (Fig. 11c) shows a doublet Ag3d consisting of two sharp and symmetrical peaks at 368.1 eV ($\text{Ag}3d_{5/2}$) and 374.2 eV ($\text{Ag}3d_{3/2}$) associated with a single species of silver at zero-oxidation state (Ag^0). The absence of oxidized silver components (silver oxide or hydroxide) could indicate that the silver particles are stabilized by the polymer with which they are in contact. Indeed, since the redox potential of the Ag^+/Ag couple (roughly 0.8 V,

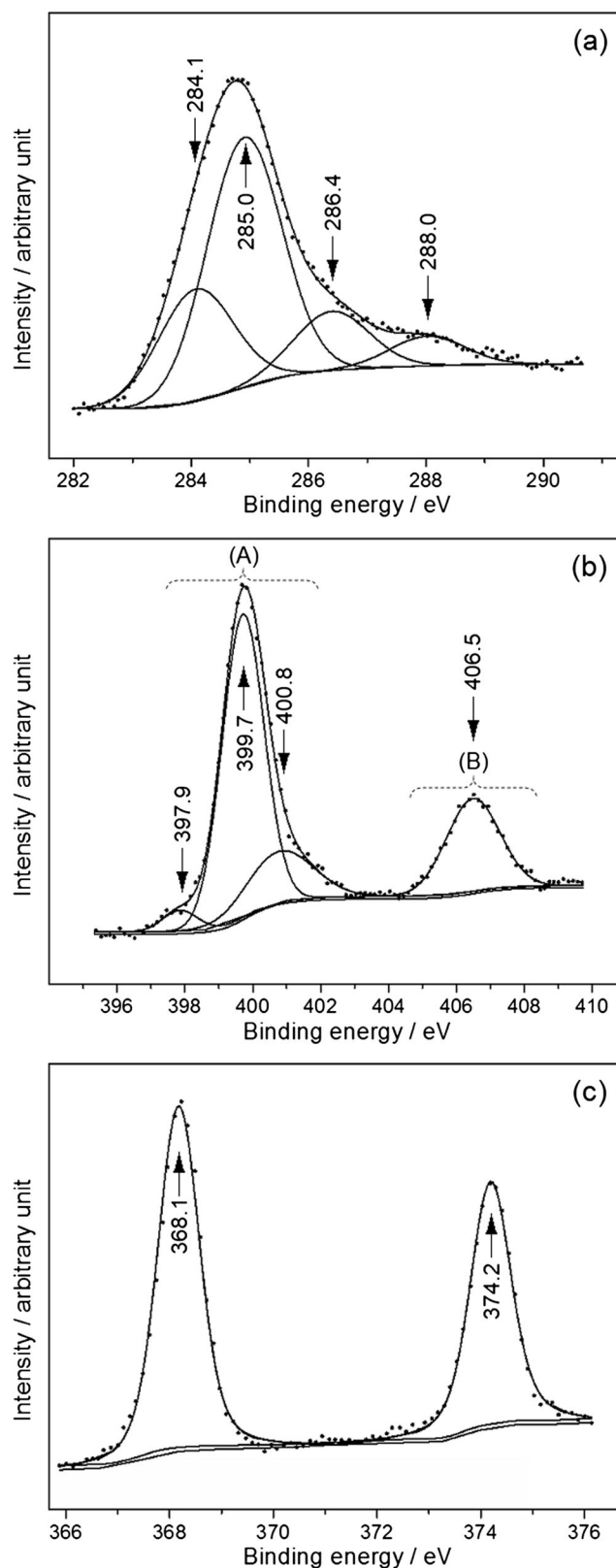


Fig. 11 XPS analysis of photochemically prepared polypyrrole with leaf-shaped Ag crystals. **a** C1s, **b** N1s, and **c** Ag3d XPS signals

depending on the activity of Ag^+) is greater than that of the $\text{PPy}^{\text{ox}}/\text{PPy}^{\text{red}}$ (located between -0.4 and -0.05 V which are

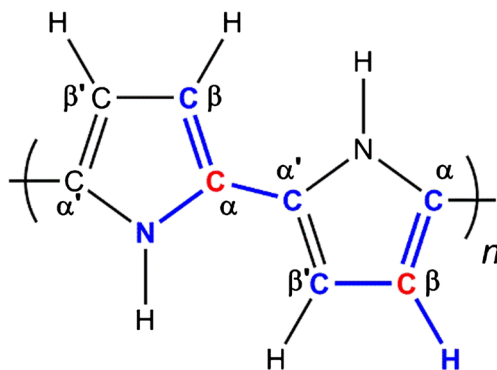
the potentials of the cathodic and anodic peaks of PPy, respectively, Fig. 4), the metallic Ag^0 and the oxidized PPy^{ox} species are the most stable thermodynamically.

The involvement of nitrate counter-ions NO_3^- in the PPy doping process and the determination of the polymer chemical composition and doping rate requires a thorough analysis of the C1s and N1s XPS spectra (Fig. 11). Thus, the decomposition of these signals into their different components is required. It provides access to the binding energies which reveal the chemical environment of each constituent and to the relative intensities whose ratios give the chemical composition and the doping degree of the polymer. The oxygen O1s signal has been voluntarily omitted since the narrow O1s spectral zone often consists of several broad and overlapping components originating from different sources such as doping anions, contaminants, residual water, etc. which hinder the deconvolution and the assignments of the oxygen spectrum.

C1s XPS signal has been processed into four Gaussian components of 1.5 eV full width at half maximum (FWHM). All given binding energies are referred to the C1s main peak at 285.0 eV attributed to carbon atoms of the pyrrole rings, more precisely those in α and α' positions of the cycle [85–90]. Knowing that the pyrrole cycle contains two types of carbon, $C_{\alpha,\alpha'}$ and $C_{\beta,\beta'}$ in α , α' and β , β' positions, respectively, with different chemical environments (Scheme 3), it is expected to observe a second band since the binding energies of the 1s electrons of the carbon nucleus in $C_{\alpha,\alpha'}$ and $C_{\beta,\beta'}$ would not be the same. Thus, the peak at 284.1 eV has been assigned in several papers to $C_{\beta,\beta'}$ 1s [85–90].

Clark et al. [91] have measured binding energies for some five membered heterocycles. They reported, in the case of pyrrole monomer, that the presence of nitrogen which is more electronegative than hydrogen leads to a shift of 0.9 eV in C1s binding energy between $C_{\alpha,\alpha'}$ and $C_{\beta,\beta'}$. This is exactly the same value we obtained in the case of PPy-Ag composite.

Ideally, the conjugated skeleton of polypyrrole contains as many $C_{\alpha,\alpha'}$ as $C_{\beta,\beta'}$. Therefore, the intensities of the two lines were expected to be of approximately the same order of



Scheme 3 The carbons at α and β positions do not have the same chemical environment: C_{α} is bonded to two carbons and one nitrogen, while C_{β} is bonded to two carbons and one hydrogen

magnitude. However, the intensity ratio $I(C_{\alpha,\alpha'})/I(C_{\beta,\beta'})$ gives a much higher value (ca. 2.2) than that intended to reflect the equal amounts of both carbon species. Contrary to Pfluger and Street [88], it is unlikely that this large difference in intensity can be explained only by the presence of hydrocarbon contamination. On the other hand, in a paper devoted to XPS investigation of electrochemically synthesized polypyrrole, Atanasoska et al. [85] reported that the greater intensity of the $C_{\alpha,\alpha'}$ arises as a consequence of some structural arrangement of doped polypyrrole and not by random contamination. In short, so far, no consistent interpretation has been stated to explain this intensity disproportion.

The coupling being mainly α - α' , one could also think of the appearance of lateral groups attached to some β carbons along the polymer backbone as has been observed in the case of other polyheterocycles [37, 40–42]. This would cause an intensity drop of the $C_{\beta,\beta'}$ 1s component. The existence of such groups, mostly oxygenated as C–OH and C=O, which act as structural defects in the polypyrrole matrix is reinforced by the presence of two other bands at 286.4 and 288.0 eV, assigned to higher oxidation states carbon atoms. However, this assumption on its own would not be enough to justify the sharp decrease of the $C_{\beta,\beta'}$ line intensity, which is about half in comparison with $C_{\alpha,\alpha'}$ component.

The peak at 286.4 eV is attributed to β C–OH species [87, 89] and carbons adjacent to positively charged nitrogen atoms α C– N^+ [87, 92]. To confirm the former attribution and to identify the source of these covalently bonded hydroxyl groups, Lei and Martin [93] carried out infrared investigations of polypyrrole and poly(N-methylpyrrole) electrochemically synthesized in acetonitrile containing traces of water. They conclude that the emergence of the –OH defects results from nucleophilic attacks by water on the growing polymer chains during the electropolymerization process. When the organic electrolytic medium is rigorously dried, the IR bands associated with these groups are not observed.

A fourth highest binding energy peak of relatively weak intensity at 288.0 eV arises from carbonyl groups β C=O [45, 87, 94–96]. They are also structural defects resulting from a slight oxidation of the polymer surface due to the unavoidable oxygen of contamination [45]. Recently, we have shown in the case of polythiophene that the amount of carbonyl groups increases with the increase of the polymer oxidation degree [97]. When the polymer is subjected to higher potentials, its electrophilic character becomes more pronounced and, hence, undergoes more nucleophilic attacks leading to more substitutions.

The XPS spectrum of nitrogen N1s (Fig. 11b) is particularly interesting, it results from the overlapping of two contributions: the nitrogen atoms of the pyrrole rings in the polymer skeleton and those belonging to the nitrate doping anions. Thus, it consists of two spectral massifs, A and B, which after signal processing into Gaussian bands, reveal the presence of four different nitrogen species.

The main band at 399.7 eV is associated with the neutral N in PPy, while positively charged nitrogen atoms N^+ come out with 400.8 eV binding energy [98]. The intensity ratio of N^+ to total nitrogen atoms belonging to PPy chains $I(N^+)/I(N_{PPy})$ can be used as an indicator of the polymer oxidation state. In our case, the calculated ratio is 0.20 (20%).

The polymer doping rate can also be calculated by the intensity ratio of the band at 406.5 eV assigned to the nitrogen of the NO_3^- counterion (B) compared to the N1s signal of the PPy skeleton (A) $I(N_{NO_3^-})/I(N_{PPy})$. A doping level of 0.29 (29%) was found, indicating that the obtained composite, stabilized by the silver particles, is in advanced oxidation state, the maximum value being 0.33 (33%). This observation will be confirmed later by surface enhanced Raman scattering analyses (see below).

It must be emphasized that the difference between the values 0.20 and 0.29 calculated using the two intensity ratios $I(N^+)/I(N_{PPy})$ and $I(N_{NO_3^-})/I(N_{PPy})$, respectively, could be due to the existence of a quantity of non-doping nitrates trapped in the polymer matrix during the polymerization process. The coexistence of two types of doping and non-doping anions has already been observed in the case of other supporting electrolytes such as perchlorates ClO_4^- and other conducting polymers such as polythiophene [97, 99, 100].

A fourth peak appears at 397.9 eV as a weak shoulder in the low-binding energy side of the massif A. It has been assigned by several authors to nitrogen of $C=N$ structural defects [45, 46, 87]. This component represents, on average, only 3.4% of the total area of the N1 s spectrum.

Effect of the fractal character of the silver crystals on the SERS enhancement factor

The SERS spectrum shown in Fig. 12 is that of PPy obtained photochemically simultaneously with the deposition of Ag on

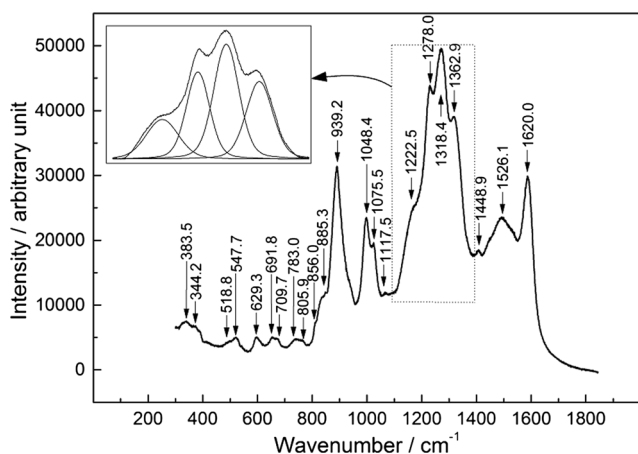


Fig. 12 SERS spectrum of polypyrrole obtained photochemically simultaneously with the deposition of fractal Ag on a Cu plate. The inset is a decomposition in four bands of the 1100–1400 cm^{-1} spectral domain. The spectrum is recorded with 514.5 nm excitation wavelength and 1 mW laser power

a Cu plate (PCP protocol). In comparison with all the Raman spectra of PPy presented so far, that of Fig. 12 is of exceptional quality. Indeed, the background noise is virtually nonexistent and the enhancement factor reaches, in this case, 200 instead of 100 obtained for PPy electrodeposited on SERS-activated Ag plate. This dramatic SERS effect is attributed to the fractal nature of the analyzed surface, in agreement with other published works [47, 48]. This point will be discussed later using FDTD simulation.

In addition, all the peaks belonging to the spectrum are highly resolved and easily discernible. In this context, the massif observed around 1300 cm^{-1} in the case of PPy/Pt and PPy/Ag appears to consist of four highly visible components in the spectrum of Fig. 12; the inset included in the same figure is a decomposition in four bands of this spectral region, which until now was impossible to perform because of the overlapping of these four Raman bands in a relatively low-resolution signal.

It should be noted that the polymer obtained by this technique has a high oxidation degree. Indeed, the $\nu_{C=C}$ band located towards the high frequencies is split into its two components at 1526 cm^{-1} and 1620 cm^{-1} in good agreement with the values calculated by Faulques et al. [65] (Table 1) and confirms what we have assumed in this context. Here, the $\nu_{C=C}^{quin.}$ line is clearly shifted towards the high frequencies and it is more intense than the $\nu_{C=C}^{arom.}$ line: this is exactly the characteristics of a PPy in an advanced oxidation state.

Unlike individual or sufficiently spaced particles and according to several papers devoted to the study of aggregated colloidal particles or branched clusters [23, 101–104], in entangled and complex structures, interstitial spaces act as localized “hot spots” where strong electromagnetic coupling occurs and leads locally to the intensification of the Raman signal. In our case, to highlight the presence of these so-called “hot spots” and qualitatively analyze the distribution and behavior of the local electromagnetic field and, therefore, the exaltation factor (EF) at these intergranular sites, we have used a finite difference time domain method (FDTD). The simulation was performed using the Lumerical FDTD Solutions software, typically on a ramified silver branch of about 300 nm length (Fig. 13) and excited at 514.5 nm.

The aim here is not to quantify the SERS enhancement factor, whose value is generally expressed as the ratio of the local field E_{loc} by the incident field E_{inc} raised to the power of four $(E_{loc}/E_{inc})^4$ [105], this could be the subject of a more detailed investigation taking into account the connections and the overlap of crystals of various sizes and shapes. The purpose is, rather, to map out, through a simple example, a spatial distribution of EF with a scale ranging from 0 (deep blue) corresponding to SERS-inactive zones to 100 (dark brown) representing the “hot spots” seats of the highest intensification of the incident field.

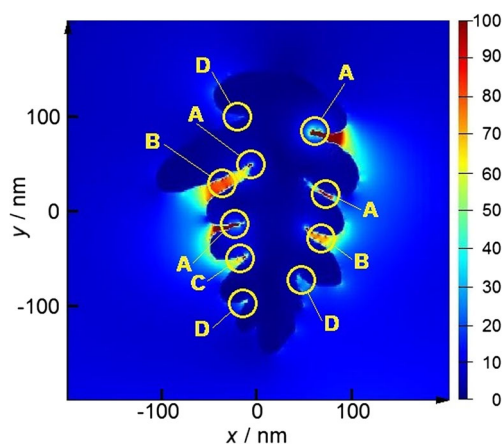


Fig. 13 FDTD simulation for a leaf-shaped silver crystal pattern. The enhancement factor in the “hot spots” decreases in the order $A > B > C > D$

Figure 13 shows the existence of several cavities more or less “hot” spread across the leaf-shaped fractal object. It follows that the PPy chains incorporated in the interstices A of a few nanometers are the most concerned by the enhancement effect of the Raman signal. It should be noted, however, that the number of these sites would be much larger if one considers the propagation of the fractal geometry and the tip effects due to the interconnections between the various entangled silver clusters.

From this set of results, it appears that the gain in intensity of the PPy SERS spectrum observed in this case in comparison with that of the film electrodeposited on a roughened massive electrode can be attributed to the fractal nature of the Ag crystal growth, which promotes the formation of “hot spots” and tips with high abundance.

Conclusion

The electropolymerization of pyrrole on roughened Ag electrode has led to an important amplification of the Raman intensity whose enhancement factor reached 100 in comparison with the resonance Raman spectrum of PPy obtained in the same conditions on Pt. This significantly improved the resolution of the PPy spectra and facilitated the identification of the various vibrational modes. According to the SERS selection rules, the intensification of the $C_{\beta}-H$ and $C-N$ modes suggests that the nuclei of the polymer are perpendicular to the surface of the electrode. This behavior, already observed in the case of other conducting polymers such as polythiophene and its derivatives, is reinforced by the strong affinity of silver for heteroatoms.

The in situ SERS experiments carried out on this polymer have enabled to follow several structural changes which accompany the transition from the reduced to the oxidized form, in particular the transformation of certain nuclei from aromatic to quinoid structure.

Moreover, the importance of the fractal behavior of the surface in the observation of SERS effect is dramatically confirmed by the analysis of PPy with a fractal distribution of Ag crystals photochemically obtained on a Cu plate. In this later case, the fractal leaf-shaped silver matrices exhibited significantly higher enhancement of the Raman intensity compared to the roughened silver plate because of the high amount of “hot spots” and tips as evidenced by a brief finite difference time domain simulation.

Funding information This work was supported by the MESRSFC and CNRST (Morocco) under grant No. PPR/30/2015.

References

1. Alvarez-Puebla RA, Liz-Marzán LM (2010) SERS-based diagnosis and biodetection. *Small* 6(5):604–610
2. Brazhe NA, Abdali S, Brazhe AR, Luneva OG, Bryzgalova NY, Parshina EY, Sosnovtseva OV, Maksimov GV (2009) New insight into erythrocyte through in vivo surface-enhanced Raman spectroscopy. *Biophys J* 97(12):3206–3214
3. Kneipp J, Kneipp H, Wittig B, Kneipp K (2007) One- and two-photon excited optical pH probing for cells using surface-enhanced Raman and hyper-Raman nanosensors. *Nano Lett* 7(9):2819–2823
4. Syme CD, Sirimuthu NM, Faley SL, Cooper JM (2010) SERS mapping of nanoparticle labels in single cells using a microfluidic chip. *Chem Commun* 46(42):7921–7923
5. Huang Z, Gu X, Cao Q, Hu P, Hao J, Li J, Tang X (2012) Catalytically active single-atom sites fabricated from silver particles. *Angew Chem* 124(17):4274–4279
6. Pradhan N, Pal A, Pal T (2002) Silver nanoparticle catalyzed reduction of aromatic nitro compounds. *Colloid Surface A* 196(2-3):247–257
7. Crooks RM, Zhao M, Sun L, Chechik V, Yeung LK (2001) Dendrimer-encapsulated metal nanoparticles: synthesis, characterization, and applications to catalysis. *Acc Chem Res* 34(3):181–190
8. Layani M, Gruchko M, Milo O, Balberg I, Azulay D, Magdassi S (2009) Transparent conductive coatings by printing coffee ring arrays obtained at room temperature. *ACS Nano* 3(11):3537–3542
9. Magdassi S, Grouchko M, Toker D, Kamyshny A, Balberg I, Millo O (2005) Ring stain effect at room temperature in silver nanoparticles yields high electrical conductivity. *Langmuir* 21(23):10264–10267
10. Kamyshny A, Ben-Moshe M, Aviezer S, Magdassi S (2005) Ink-jet printing of metallic nanoparticles and microemulsions. *Macromol Rapid Commun* 26(4):281–288
11. Pietrobon B, Kitaev V (2008) Photochemical synthesis of monodisperse size-controlled silver decahedral nanoparticles and their remarkable optical properties. *Chem Mater* 20(16):5186–5190
12. Leopold N, Lendl B (2003) A new method for fast preparation of highly surface-enhanced Raman scattering (SERS) active silver colloids at room temperature by reduction of silver nitrate with hydroxylamine hydrochloride. *J Phys Chem B* 107(24):5723–5727
13. Moskovits M (2005) Surface-enhanced Raman spectroscopy: a brief retrospective. *J Raman Spectrosc* 36(6-7):485–496
14. Gong X, Bao Y, Qiu C, Jiang C (2012) Individual nanostructured materials: fabrication and surface-enhanced Raman scattering. *Chem Commun* 48(56):7003–7018

15. Fleischmann M, Hendra PJ, McQuillan AJ (1974) Raman spectra of pyridine adsorbed at a silver electrode. *Chem Phys Lett* 26(2): 163–166
16. Kneipp K, Wang Y, Kneipp H, Itzkan I, Dasari RR, Feld MS (1996) Population pumping of excited vibrational states by spontaneous surface-enhanced Raman scattering. *Phys Rev Lett* 76(14):2444–2447
17. Emory SR, Haskins WE, Nie S (1998) Direct observation of size-dependent optical enhancement in single metal nanoparticles. *J Am Chem Soc* 120(31):8009–8010
18. Krug JT, Wang GD, Emory SR, Nie S (1999) Efficient Raman enhancement and intermittent light emission observed in single gold nanocrystals. *J Am Chem Soc* 121(39):9208–9214
19. Gunnarsson L, Petronis S, Kasemo B, Xu H, Bjerneld J, Käll M (1999) Optimizing nanofabricated substrates for surface enhanced Raman scattering. *Nanostruct Mater* 12(5-8):783–788
20. Eliasson C, Lorén A, Murty KVGK, Josefson M, Käll M, Abrahamsson J, Abrahamsson K (2001) Multivariate evaluation of doxorubicin surface-enhanced Raman spectra. *Spectrochim Acta A* 57(9):1907–1915
21. Nie S, Emory SR (1997) Probing single molecules and single nanoparticles by surface-enhanced Raman scattering. *Science* 275(5303):1102–1106
22. Kneipp K, Wang Y, Kneipp H, Perelman LT, Itzkan I, Dasari RR, Feld MS (1997) Single molecule detection using surface-enhanced Raman scattering (SERS). *Phys Rev Lett* 78(9):1667–1670
23. Kneipp K, Kneipp H, Kartha VB, Manoharan R, Deinum G, Itzkan I, Dasari RR, Feld MS (1998) Detection and identification of a single DNA base molecule using surface-enhanced Raman scattering (SERS). *Phys Rev E* 57:6281–6284
24. Xu H, Bjerneld EJ, Käll M, Börjesson L (1999) Spectroscopy of single hemoglobin molecules by surface enhanced Raman scattering. *Phys Rev Lett* 83(21):4357–4360
25. Michaels AM, Jiang J, Brus L (2000) Ag nanocrystal junctions as the site for surface-enhanced Raman scattering of single rhodamine 6G molecules. *J Phys Chem B* 104(50):11965–11971
26. Bosnick KA, Jiang J, Brus LE (2002) Fluctuations and local symmetry in single-molecule rhodamine 6G Raman scattering on silver nanocrystal aggregates. *J Phys Chem B* 106(33):8096–8099
27. Moskovits M (1985) Surface-enhanced spectroscopy. *Rev Mod Phys* 57(3):783–826
28. Shalaev VM, Stockman MI, Botet R (1992) Resonant excitations and nonlinear optics of fractals. *Physica A* 185(1-4):181–186
29. Shalaev VM, Botet R, Tsai DP, Kovacs J, Moskovits M (1994) Fractals: localization of dipole excitations and giant optical polarizabilities. *Physica A* 207(1-3):197–207
30. Stockman MI, Pandey LN, Muratov LS, George TF (1994) Giant fluctuations of local optical fields in fractal clusters. *Phys Rev Lett* 72(15):2486–2489
31. Shalaev VM, Botet R, Mercier J, Stechel EB (1996) Optical properties of self-affine thin films. *Phys Rev B* 54(11):8235–8242
32. Stockman MI (1997) Inhomogeneous eigenmode localization, chaos, and correlations in large disordered clusters. *Phys Rev E* 56(6):6494–6507
33. Shalaev VM, Sarychev AK (1998) Nonlinear optics of random metal-dielectric films. *Phys Rev B* 57(20):13265–13288
34. Grésillon S, Aigouy L, Boccaro AC, Rivoal JC, Quelin X, Desmarest C, Gadenne P, Shubin AV, Sarychev AK, Shalaev VM (1999) Experimental observation of localized optical excitations in random metal-dielectric films. *Phys Rev Lett* 82(22): 4520–4523
35. Su X, Zhang J, Sun L, Koo TW, Chan S, Sundararajan N, Yamakawa M, Berlin AA (2005) Composite organic–inorganic nanoparticles (COINs) with chemically encoded optical signatures. *Nano Lett* 5(1):49–54
36. Stuart DA, Yonzon CR, Zhang X, Lyandres O, Shah NC, Glucksberg MR, Walsh JT, Van Duyne RP (2005) Glucose sensing using near-infrared surface-enhanced Raman spectroscopy: gold surfaces, 10-day stability, and improved accuracy. *Anal Chem* 77(13):4013–4019
37. Bazaoui EA, Levi G, Aeiyaeh S, Aubard J, Marsault JP, Lacaze PC (1995) SERS spectra of polythiophene in doped and undoped states. *J Phys Chem* 99(17):6628–6634
38. Bazaoui EA, Aeiyaeh S, Aubard J, Felidj N, Lacaze PC, Sakmeche N, Levi G (1998) Electrochemical procedure for obtaining surface-enhanced Raman scattering active polythiophene films on platinum. *J Raman Spectrosc* 29(3):177–183
39. Bazaoui EA, Aeiyaeh S, Aubard J, Felidj N, Levi G, Sakmeche N, Lacaze PC (1998) New electrochemical procedure for obtaining surface enhanced Raman scattering active polythiophene films on platinum. *J Chim Phys Physicochim Biol* 95(6):1526–1530
40. Bazaoui EA, Bazaoui M, Aubard J, Lomas JS, Félidj N, Lévi G (2001) Surface-enhanced Raman scattering study of polyalkylthiophenes on gold electrodes and in silver colloids. *Synth Met* 123(2):299–309
41. Bazaoui EA, Aubard J, Felidj N, Laurent G, Levi G (2005) Ex situ and in situ SERS analyses of polybithiophene using roughened Ag and Cu electrodes and multilayer SERS-active systems. *J Raman Spectrosc* 36(8):817–823
42. Bazaoui EA, Aubard J, Bazaoui M, Lévi G (2007) Application of surface-enhanced Raman scattering for ex situ and in situ investigations of Polythiophene derivatives. *Spectrosc Lett* 40(5): 723–740
43. Aouzal Z, Bouabdallaoui M, Jadi SB, El Jaouhari A, Bazaoui M, Wang R, Bazaoui EA (2017) In situ surface-enhanced Raman scattering investigation of poly (5-amino-1, 4-naphthoquinone) using roughened electrodes and metal colloids. *Synth Met* 231: 80–88
44. Sakamoto M, Fujituka M, Majima T (2009) Light as a construction tool of metal nanoparticles: synthesis and mechanism. *J Photochem Photobiol C* 10(1):33–56
45. Singh A, Salmi Z, Joshi N, Jha P, Decorse P, Lecoq H, Lau-Truong S, Jouini M, Aswal DK, Chehimi MM (2013) Electrochemical investigation of free-standing polypyrrole–silver nanocomposite films: a substrate free electrode material for supercapacitors. *RSC Adv* 3(46):24567–24575
46. Zang L, Qiu J, Yang C, Sakai E (2016) Preparation and application of conducting polymer/Ag/clay composite nanoparticles formed by in situ UV-induced dispersion polymerization. *Sci Rep* 6(1): 20470–20182
47. Claro F, Fuchs R (1991) Collective surface modes in a fractal cluster of spheres. *Phys Rev B* 44(9):4109–4116
48. Stockman MI, Shalaev VM, Moskovits M, Botet R, George TF (1992) Enhanced Raman scattering by fractal clusters: scale-invariant theory. *Phys Rev B* 46(5):2821–2830
49. Gersten J, Nitzan A (1981) Spectroscopic properties of molecules interacting with small dielectric particles. *J Chem Phys* 75(3): 1139–1152
50. Moskovits M (1978) Surface roughness and the enhanced intensity of Raman scattering by molecules adsorbed on metals. *J Chem Phys* 69(9):4159–4161
51. McCall SL, Platzman PM, Wolff PA (1980) Surface enhanced Raman scattering. *Phys Lett A* 77(5):381–383
52. Rojas R, Claro F (1993) Theory of surface enhanced Raman scattering in colloids. *J Chem Phys* 98(2):998–1006
53. Aravind PK, Metiu H (1980) The enhancement of Raman and fluorescent intensity by small surface roughness. Changes in dipole emission. *Chem Phys Lett* 74(2):301–305

54. Aroca R (2006) Surface-enhanced vibrational spectroscopy. John Wiley & Sons
55. Shalaev VM (1996) Electromagnetic properties of small-particle composites. *Phys Rep* 272(2-3):61–137
56. Roy PK, Huang YF, Chattopadhyay S (2013) Detection of melamine on fractals of unmodified gold nanoparticles by surface-enhanced Raman scattering. *J Biomed Opt* 19(1):011002
57. Amarandei G, O'Dwyer C, Arshak A, Corcoran D (2013) Fractal patterning of nanoparticles on polymer films and their SERS capabilities. *ACS Appl Mater Interfaces* 5(17):8655–8662
58. Hou C, Meng G, Huang Q, Zhu C, Huang Z, Chen B, Sun K (2014) Ag-nanoparticle-decorated au-fractal patterns on bowl-like-dimple arrays on Al foil as an effective SERS substrate for the rapid detection of PCBs. *Chem Commun* 50(5):569–571
59. Qiu T, Wu XL, Shen JC, Xia Y, Shen PN, Chu PK (2008) Silver fractal networks for surface-enhanced Raman scattering substrates. *Appl Surf Sci* 254(17):5399–5402
60. Xu D, Dong J, Zhang S, Chen J (2018) Fractal theory study and SERS effect of centimeter level of copper nanobranched detectors by solid-state ionic method. *Sensors Actuators A Phys* 271:18–23
61. Rodriguez I, Scharifker BR, Mostany J (2000) In situ FTIR study of redox and overoxidation processes in polypyrrole films. *J Electroanal Chem* 491(1-2):117–125
62. Otero TF, Marquez M, Suarez IJ (2004) Polypyrrole: diffusion coefficients and degradation by overoxidation. *J Phys Chem B* 108(39):15429–15433
63. Fernández I, Trueba M, Nunez CA, Rieumont J (2005) Some features of the overoxidation of polypyrrole synthesized on austenitic stainless steel electrodes in aqueous nitrate solutions. *Surf Coat Technol* 191(1):134–139
64. Liu AS, Oliveira MA (2007) Electrodeposition of polypyrrole films on aluminum from tartrate aqueous solution. *J Braz Chem Soc* 18(1):143–152
65. Faulques E, Wallnöfer W, Kuzmany H (1989) Vibrational analysis of heterocyclic polymers: a comparative study of polythiophene, polypyrrole, and polyisothianaphthene. *J Chem Phys* 90(12):7585–7593
66. Hagiwara T, Hirasaka M, Sato K, Yamaura M (1990) Enhancement of the electrical conductivity of polypyrrole film by stretching: influence of the polymerization conditions. *Synth Met* 36(2):241–252
67. Liu YC, Hwang BJ (2000) Identification of oxidized polypyrrole on Raman spectrum. *Synth Met* 113(1-2):203–207
68. Ye S, Fang L, Lu Y (2009) Contribution of charge-transfer effect to surface-enhanced IR for ag@ PPy nanoparticles. *Phys Chem Chem Phys* 11(14):2480–2484
69. Nuzzo RG, Allara DL (1983) Adsorption of bifunctional organic disulfides on gold surfaces. *J Am Chem Soc* 105(13):4481–4483
70. Li TT, Weaver MJ (1984) Intramolecular electron transfer at metal surfaces. 4. Dependence of tunneling probability upon donor-acceptor separation distance. *J Am Chem Soc* 106(20):6107–6108
71. Nuzzo RG, Fusco FA, Allara DL (1987) Spontaneously organized molecular assemblies. 3. Preparation and properties of solution adsorbed monolayers of organic disulfides on gold surfaces. *J Am Chem Soc* 109(8):2358–2368
72. Finklea HO, Avery S, Lynch M, Furtch T (1987) Blocking oriented monolayers of alkyl mercaptans on gold electrodes. *Langmuir* 3(3):409–413
73. Porter MD, Bright TB, Allara DL, Chidsey CE (1987) Spontaneously organized molecular assemblies. 4. Structural characterization of n-alkyl thiol monolayers on gold by optical ellipsometry, infrared spectroscopy, and electrochemistry. *J Am Chem Soc* 109(12):3559–3568
74. Stouffer JM, McCarthy TJ (1988) Polymer monolayers prepared by the spontaneous adsorption of sulfur-functionalized polystyrene on gold surfaces. *Macromolecules* 21(5):1204–1208
75. Bell RA, Kramer JR (1999) Structural chemistry and geochemistry of silver-sulfur compounds: critical review. *Environ Toxicol Chem* 18:9–22
76. Nath S, Ghosh SK, Kundu S, Praharaj S, Panigrahi S, Pal T (2006) Is gold really softer than silver? HSAB principle revisited. *J Nanopart Res* 8(1):111–116
77. Nair S, Tatarchuk BJ (2010) Supported silver adsorbents for selective removal of sulfur species from hydrocarbon fuels. *Fuel* 89(11):3218–3225
78. Bukowska J, Jackowska K (1990) In situ Raman studies of polypyrrole and polythiophene films on Pt electrodes. *Synth Met* 35(1-2):143–150
79. Meisterle P, Kuzmany H, Nauer G (1984) In situ Raman spectroscopy of the electrochemical doping process in polyacetylene. *Phys Rev B* 29(10):6008–6011
80. Kuzmany H (1985) The particle in the box model for resonance Raman scattering in polyacetylene. *Pure Appl Chem* 57(2):235–246
81. Marsault JP, Fraoua K, Aeiyaeh S, Aubard J, Levi G, Lacaze PC (1992) Étude structurale par spectrométrie Raman in situ de films minces de polypyrrole électropolymérisé sur différents substrats. *J Chim Phys* 89:1167–1172
82. Virdee HR, Hester RE (1988) In situ resonance Raman spectroscopic investigation of a Polypyrrole modified gold electrode. *Croat Chem Acta* 61:357–374
83. Liu YC, Yang KH, Lin LH, Tsai JF (2008) Studies of thermal decay of electropolymerized polypyrrole using in situ surface-enhanced Raman spectroscopy. *Electrochem Commun* 10(1):161–164
84. Schantz S, Torell LM, Stevens JR (1988) Raman and Brillouin scattering of LiClO₄ complexed in poly(propylene-glycol). *J Appl Phys* 64(4):2038–2043
85. Atanasoska L, Naoi K, Smyrl WH (1992) XPS studies on conducting polymers: polypyrrole films doped with perchlorate and polymeric anions. *Chem Mater* 4(5):988–994
86. Dong S, Ding J (1987) Study on polypyrrole film by electrochemical polymerization in aqueous solution. *Synth Met* 20(1):119–124
87. Liang W, Lei J, Martin CR (1992) Effect of synthesis temperature on the structure, doping level and charge-transport properties of polypyrrole. *Synth Met* 52(2):227–239
88. Pfluger P, Street GB (1984) Chemical, electronic, and structural properties of conducting heterocyclic polymers: a view by XPS. *J Chem Phys* 80(1):544–553
89. Ribó JM, Dicko A, Tura JM, Bloor D (1991) Chemical structure of polypyrrole: X-ray photoelectron spectroscopy of polypyrrole with 5-yliden-3-pyrrolin-2-one end groups. *Polymer* 32(4):728–732
90. Tabačiarová J, Mičušík M, Fedorko P, Omastová M (2015) Study of polypyrrole aging by XPS, FTIR and conductivity measurements. *Polym Degrad Stab* 120:392–401
91. Clark DT, Lilley DMJ (1971) Molecular core binding energies for some five membered ring heterocycles as determined by X-ray photoelectron spectroscopy. *Chem Phys Lett* 9(3):234–237
92. Eaves JG, Munro HS, Parker D (1987) An ESCA study of polypyrrole oxidation. *Polym Commun* 28:38–40
93. Lei J, Liang W, MCR (1992) Infrared investigations of pristine, doped and partially doped polypyrrole. *Synth Met* 48(3):301–312
94. Ferreira CA, Aeiyaeh S, Delamar M, Lacaze PC (1990) Electropolymerization of pyrrole on iron electrodes: influence of solvent and electrolyte on the nature of the deposits. *J Electroanal Chem* 284:351–369
95. Zaid B, Aeiyaeh S, Lacaze PC (1994) Electropolymerization of pyrrole in propylene carbonate on zinc electrodes modified by heteropolyanions. *Synth Met* 65(1):27–34

96. Schweiger B, Kim J, Kim YJ, Ulbricht M (2015) Electropolymerized molecularly imprinted polypyrrole film for sensing of clofibric acid. *Sensors* 15(3):4870–4889
97. Bouabdallaoui M, Aouzal Z, Ben Jadi S, El Jaouhari A, Bazzaoui M, Lévi G, Aubard J, Bazzaoui EA (2017) X-ray photoelectron and in situ and ex situ resonance Raman spectroscopic investigations of polythiophene overoxidation. *J Solid State Electrochem* 21(12):3519–3532
98. Chang M, Kim T, Park HW, Kang M, Reichmanis E, Yoon H (2012) Imparting chemical stability in nanoparticulate silver via a conjugated polymer casing approach. *ACS Appl Mater Interfaces* 4(8):4357–4365
99. Morea G, Sabbatini L, Zambonin PG, Swift AJ, West RH, Vickerman JC (1991) Modification of polybithiophene by electrochemical cycling studied by ToF-SIMS and XPS. *Macromolecules* 24(12):3630–3637
100. Morea G, Sabbatini L, West RH, Vickerman JC (1992) Surface characterization (XPS and SIMS) of emersed polybithiophene electrodes. *Surf Interface Anal* 18(6):421–429
101. Lin H, Mock J, Smith D, Gao T, Sailor MJ (2004) Surface-enhanced Raman scattering from silver-plated porous silicon. *J Phys Chem B* 108(31):11654–11659
102. Hao E, Bailey RC, Schatz GC, Hupp JT, Li S (2004) Synthesis and optical properties of “branched” gold nanocrystals. *Nano Lett* 4(2):327–330
103. Talley CE, Jackson JB, Oubre C, Grady NK, Hollars CW, Lane SM, Huser TH, Nordlander P, Halas NJ (2005) Surface-enhanced Raman scattering from individual au nanoparticles and nanoparticle dimer substrates. *Nano Lett* 5(8):1569–1574
104. Kneipp J, Kneipp H, McLaughlin M, Brown D, Kneipp K (2006) In vivo molecular probing of cellular compartments with gold nanoparticles and nanoaggregates. *Nano Lett* 6(10):2225–2231
105. Xu H (2004) Theoretical study of coated spherical metallic nanoparticles for single-molecule surface-enhanced spectroscopy. *Appl Phys Lett* 85(24):5980–5982

Publisher's note Springer Nature remains neutral with regard to jurisdictional claims in published maps and institutional affiliations.